Recent Advances in the Operational Vicarious Calibration of Visible and Near-infrared Ocean Color Satellite Radiometry

P. Jeremy Werdell[1,4], Bryan A. Franz[2,4], Sean W. Bailey[3,4], and Charles R. McClain[4]

[1]Science Systems and Applications Inc., Lanham, Maryland
[2]Science Applications International Corporation, San Diego, California
[3]Futuretech Corporation, Greenbelt, Maryland
[4]NASA Goddard Space Flight Center, Greenbelt, Maryland

INTRODUCTION

Satellite ocean color data records provide the research community a means of studying the Earth's climate and marine biosphere on spatial and temporal scales unattainable via conventional *in situ* methods. The Sea-viewing Wide Field-of-View Sensor (SeaWiFS) and Moderate Resolution Imaging Spectroradiometer (MODIS-Aqua), for example, have supplied the oceanographic community continuous, global marine bio-optical data sets since 1997 and 2002, respectively. The community now relies heavily on their data products to support studies ranging from management of regional ecosystems[1] to development of decadal climate records[2]. The utility of SeaWiFS and MODIS-Aqua results in part from their on-orbit vicarious calibration, executed by the NASA Ocean Biology Processing Group (OBPG), to account for the integrated instrument-atmosphere correction system[3,4]. Here, we describe several recent advances in the operational OBPG vicarious calibration approach for ocean color satellite visible and NIR radiometry.

Satellite-borne ocean color sensors measure the visible and near-infrared (NIR) radiance exiting the top of the atmosphere, $L_t(\lambda)$. Semi-analytical algorithms are required to retrieve the portion of that signal that exits the sea surface[5]. The desired uncertainties on this water-leaving radiance, $L_w(\lambda)$, cannot be achieved through pre-launch laboratory calibration and characterizations alone[3]. For example, the pre-launch calibration uncertainties for SeaWiFS are approximately 3% of the $L_t(\lambda)$ signal[4], with the $L_w(\lambda)$ signal contributing roughly 10% of this signal in the blue-green spectral regime. As such, even for very clear oligotrophic conditions, the relative error of the pre-launch calibration approaches 20 – 40%[6] for $L_w(\lambda)$, which is well above the stated goal of 5% for the retrieval at 443-nm[7]. To retrieve water-leaving radiances at this strict uncertainty level, ocean color sensors require additional on-orbit calibration.

In the vicarious calibration, the OBPG derives fractional gain factors (with values of unity indicating no adjustment to the pre-launch calibration) by forcing the satellite visible and NIR radiances to agree with "ground truth" normalized water-leaving radiances, $L_{wn}(\lambda)$, and assumed atmospheric aerosol conditions, respectively. It is also assumed that temporal trends in the sensor response have been accurately removed *a priori* using lunar and solar diffuser observations[8]. During operational data processing, the gain factors are applied to $L_t(\lambda)$, effectively updating the pre-launch calibration to account for undetermined post-launch changes to the instrument and biases associated with the atmospheric correction. We should note that the methodology described here does not presume anything about the heritage of the ground truth $L_w(\lambda)$ targeted for calibration. For example, while the

OBPG currently uses $L_{wn}(\lambda)$ from the Marine Optical Buoy (MOBY)[9] for the visible band vicarious calibration, the approach generically permits the use of $L_{wn}(\lambda)$ from regional climatologies, models, or another remote sensor.

THE VICARIOUS CALIBRATION APPROACH

To describe the vicarious calibration process, it is useful to review the components of the Gordon and Wang[5,10,11] atmospheric correction algorithm, where $L_t(\lambda)$ provide the input and $L_w(\lambda)$ are the output:

$$L_t = \left(L_r + L_a + t_{dv}L_f + t_{dv}L_w\right)t_{gv}t_{gs}f_p \tag{1}$$

Spectral dependence is hereafter implied and the variables are defined in Table 1. The unknown terms in (1) are L_w and L_a, with the latter also effecting the determination of t_d. The remaining terms are computed *a priori* or reliably estimated given the radiant path geometries. The atmospheric correction scheme assumes L_w to be negligible in the NIR, such that the unknown terms reduce to L_a in this spectral regime. When L_a is known at two NIR bands, as is the case when L_w(NIR) is set to zero, the aerosol type and concentration are retrieved, and the selected models are used to determine L_a in the visible bands[5]. The retrieved L_w are subsequently normalized to the scenario of a non-attenuating atmosphere with the Sun directly overhead at a distance of 1 AU:

$$L_{wn} = L_w\left(\mu_s t_{ds} f_s f_b f_\lambda\right)^{-1} \tag{2}$$

The vicarious calibration process is effectively just an inversion of this forward processing algorithm, wherein known L_{wn} (denoted L_{wn}^t) provide the input and predicted L_t (denoted L_t^t) become the output. The ratio of predicted-to-observed L_t is the vicarious gain, g: the correction factor that when applied to the observed L_t would force the system to yield the expected L_{wn}:

$$L_{wn}^t = L_w^t\left(\mu_s^t t_{ds}^t f_s^t f_b^t f_\lambda^t\right)^{-1} \tag{3}$$

$$L_t^t = \left\{L_r + L_a + t_{dv}L_f + t_{dv}L_{wn}^t\left(\mu_s t_{ds} f_s f_b f_\lambda\right)\right\}t_{gv}t_{gs}f_p \tag{4}$$

$$g = L_t^t\, L_t^{-1} \tag{5}$$

The terms in parentheses in (3) may differ from those in (2) because of differences in the solar and view path geometries between the satellite observation and the target value of L_w^t if, for example, the observations were collected at different times of day. Note also that this approach differs from early SeaWiFS calibration efforts[4], where both visible and NIR vicarious gains were calculated via iterative comparison of satellite and target L_{wn}.

The atmospheric diffuse transmittance for the target, t_{ds}^t, is obtained either from *in situ* observations or derived from the satellite retrieval via:

$$t_{ds}^t = \exp\left\{-\ln\left(t_{ds}\right)\mu\,\mu^{-t}\right\} \tag{6}$$

Total diffuse transmittance, t_{ds}^t, is a product of Rayleigh and aerosol transmittances and, therefore, is dependent upon aerosol properties. As our purpose is to calibrate the instrument-algorithm system, the use of (6) in deriving t_{ds}^t is advantageous in that it ensures that L_w and L_w^t are normalized with a common atmosphere, based on aerosol properties retrieved by the atmospheric correction algorithm.

Two other terms in (2) and (3) merit further description, as they serve to normalize the target and observed radiometry. First, f_λ and f_λ^t adjust L_{wn} for satellite spectral band-pass effects[10]. All terms in (1) are computed for the full relative spectral response of each sensor band. The f_λ terms convert the full-band L_{wn} to a nominal center wavelength value, effectively removing residual out-of-band response. In the general case, f_λ^t is used to shift L_{wn}^t to the band-pass of the sensor to be calibrated. If L_w^t is measured over a narrow band-pass at the nominal center wavelengths of the satellite sensor, then f_λ^t is unity. When obtained from a hyperspectral instrument[9], L_w^t is convolved with the relative spectral response of the sensor to be calibrated and the f_λ terms are dropped in (2) and (3).

Second, f_b accounts for how an anisotropic near-surface light field influences L_{wn} as a function of solar and sensor viewing geometry and the inherent optical properties (IOPs) of the water column (e.g., the absorption and backscattering coefficients). The operational algorithm[12] to estimate f_b uses the concentration of the phytoplankton pigment chlorophyll *a*, C_a, as a proxy for IOPs. If a concentration is unavailable, it is computed from L_{wn}^t via an appropriate standard C_a algorithm, for example, OC4v4 for SeaWiFS and OC3M for MODIS-Aqua[13]. To disable this correction, f_b is spectrally set to unity.

NEAR-INFRARED BAND IMPLEMENTATION

The vicarious calibration, as described above, requires L_a^t to be known for each L_{wn}^t. Our approach takes advantage of how, within the Gordon and Wang[5] atmospheric correction process, the visible L_a and t_d are fully dependent on the NIR radiances. Following, we first calibrate the NIR bands, then use the aerosol properties (retrieved as part of the calibration) to reduce (1) to one unknown term, L_w, in each visible band. In this Section we describe the implementation of the former; the latter is outlined in the following Section.

We begin with two simplifying assumptions. First, that L_w(NIR) is truly negligible at specific target sites (e.g., those presented in Figure 2). With this assumption, (1) and (4) reduce to:

$$L_t = \left(L_r + L_a + t_{dv} L_f\right) t_{gv} t_{gs} f_p \tag{7}$$

$$L_t^t = \left(L_r + L_a^t + t_{dv} L_f\right) t_{gv} t_{gs} f_p \tag{8}$$

where L_a is the only significant unknown term (t_d for L_f is estimated based solely on a Rayleigh atmosphere in both the forward and inverse processes). Second, we assume that the instrument calibration of the longer NIR band (865 and 869-nm for SeaWiFS and MODIS-Aqua, respectively) is perfect, such that *g* is unity, the validity of which is discussed elsewhere[14,15]. Wang and Gordon[16] demonstrated that calibration of 865-nm to within 10% is sufficient to retrieve accurate L_w.

With these assumptions, our objective becomes the calibration of the shorter NIR band. In Gordon and Wang[5], the ratio of L_a in the two NIR bands determines the aerosol type, which if known, can be used in combination with L_a in the longer NIR band to determine L_a in the shorter band. Then, using (8) and (5), L_t^t can be predicted and compared with L_t to generate g for the shorter NIR band.

This process is completely independent of the visible band calibration, so the Earth location of the NIR calibration sites need not be coincident with the visible band calibration sites. Ideally, each location would maintain a stable and predictable aerosol type, preferably resulting from purely maritime processes (e.g., sea salt and water vapor). Open ocean locations usually help satisfy our first assumption, as well. Once locations have been selected, the cloud and glint-free observations are identified, and a fixed aerosol model is used to compute g for each observation date. The individual g are averaged to determine the mean vicarious gain, $\overline{g}$, for the shorter NIR band (Tables 2 and 3):

$$\overline{g} = \frac{\sum g}{n} \tag{9}$$

While the use of *in situ* aerosol observations was explored[17], the OBPG currently uses two deep ocean sites for the NIR band calibration, the South Pacific Gyre and Southern Indian Ocean (Figure 1), with the maritime aerosol model at 90% relative humidity.

VISIBLE BAND IMPLEMENTATION

In the preceding Section, we attempted to maintain a degree of generality, as our approach to vicarious calibration is independent of the particular satellite sensor and source of the calibration target data. While the same is true for the visible band calibration, in this Section, we allude more regularly to a specific example. The OBPG uses the hyperspectral L_w from MOBY[9] to calibrate space-borne visible radiometry. As the MOBY Operations Team[18] (MOT) provides quality-controlled L_w to the OBPG, we will not expand greatly on MOBY data acquisition and processing methods. It should be noted that these L_w are convolved *a priori* with the spectral band-pass of the satellite to be calibrated.

Cloud and glint-free satellite observations are first identified for each observation date. The now-calibrated NIR bands are used to determine the local aerosol type and concentration[5] and subsequently estimate L_a for the visible bands. Then, using (4) and (5), L_t^t can be predicted and compared with L_t to generate g for the visible bands. As for the NIR, the individual g are averaged to determine $\overline{g}$ for the visible bands (Tables 2 and 3, Figures 2 – 4).

Exclusion criteria are applied to both the satellite and target data prior to inclusion in the calibration scheme described above. Bailey and Werdell[19] describe the criteria used to identify viable satellite scenes in the OBPG data product validation activity (see their Figure 1). We supplement these metrics by further limiting valid scenes to those: (a) with average $C_a \leq 0.25$ mg m^{-3}; (b) with aerosol optical thickness at 865-nm ≤ 0.20; and, without any masked pixels in the 5x5 box. We also visually inspect the surrounding pixels in each scene for undetected clouds (usually, high cirrus) and biological and atmospheric homogeneity. Similar methods might be considered when L_{wn}^t are derived from a

remotely-sensed source. For MOBY, as would also be true for other *in situ* sources, we exclude observations with indications of an inhomogeneous water column or cloudy skies.

DISCUSSION

While the OBPG maintains responsibility for the vicarious calibration of MODIS-Aqua, we limit our presentation of results to SeaWiFS for brevity. Although not shown, the results for MODIS-Aqua exhibit similar behavior. First, g remains relatively stable as a function of time, both long-term and seasonally (Figure 2). This corroborates the temporal calibration of the instrument[8] and suggests consistency amongst the MOBY deployments (the MOT alternately deploys two mooring platforms for several months at a time). The scatter of g (e.g., ~5% for 443-nm), however, further underscores the need for independent lunar or solar temporal calibration, as small trends are not detectable with this approach (SeaWiFS 443-nm has degraded ~2% since launch). Similarly, g is consistent with both solar and satellite zenith angles (Figures 3 and 4, respectively). While not evident in these trends, variations with geometry would suggest problems with the atmospheric correction algorithm or with the calculation of f_b. Variations with solar geometry might also arise from complexities in the *in situ* determination of L_w under certain sky conditions, resulting from, for example, instrument self-shading by the mooring platform or wave focusing and defocusing in high light conditions.

Naturally, uncertainties stem from several places within our approach, some of which are readily quantifiable, but many of which are currently not. As a means of estimating first-order, fundamental uncertainties, we incorporate $\overline{g}$ into the OBPG satellite data product validation system[19] and calculate radiometric 'match-up' statistics for the satellite and *in situ* observations used to derive $\overline{g}$ (Table 3). While such an analysis cannot be used to truly validate the satellite retrievals, the results do provide some insight into the uncertainties associated with both the gain determination and the validation process. When executed properly, the satellite-to-*in situ* mean ratios and biases approach unity and zero, respectively, as indicated in Table 3. The absolute median percent differences, MPD, and standard deviations (root mean square), however, are not entirely negligible when considering the SeaWiFS radiometric accuracy goal of 5%[7] and the conventional means of assessing progress towards this goal. For comparison, Bailey and Werdell[19] report a MPD of 13% for SeaWiFS 443-nm for a global, deep water data set, whereas we calculate an MPD of 2% at 443-nm for the calibration data set.

We additionally review changes in $\overline{g}$ as new L_{wn}^t become available (Figure 5). As the sample sizes increase, the standard deviations (errors) of $\overline{g}$ decrease to 0.1% for 443 and 555-nm, yet the variability in range with time (minimum versus maximum g) approaches 0.5% for both. All bands maintain an ascending slope, suggesting residual drift in the satellite that is not accounted for by the temporal calibration, or possibly, a temporal drift in MOBY (although, a more likely explanation is the inclusion of anomalously low g values in 1998 that maintain some statistical influence on $\overline{g}$). The initial rapid descent in $\overline{g}$ (sample sizes less than 10) likely results from the rapid degradation of SeaWiFS in the early part of its mission, where the temporal calibration is least reliable.

The OBPG periodically reprocesses the full SeaWiFS data record when algorithms are significantly improved or MOBY data are revised. Each reprocessing includes an update to the vicarious gain, and changes of several percent are common. While these changes result from modifications of the

instrument-atmospheric correction system (in contrast to, for example, changing the source of L_{wn}^{t}), motives for reprocessing are often model and observation driven and, therefore, always include inherent uncertainties. In Table 4, we show how removing the bidirectional reflectance distribution correction (when f_b is set to unity) changes the derived $\overline{g}$. Our purpose in including this Table is twofold: (1) to provide an example of the magnitude change in $\overline{g}$ that might result from the inclusion or removal of an additional algorithm; and (b) to suggest that relative spectral changes in $\overline{g}$ that result from uncertainties in such algorithms might introduce downstream differences in retrieved C_a. Both OC4v4 and OC3M[13] use a radiometric ratio of 443 to 555-nm to estimate C_a in oligotrophic water. Given their sinusoidal form, a change of 5% in this radiometric ratio can translate into C_a changes of 10 – 20% in oligotrophic conditions.

We conclude by listing several unmentioned sources of uncertainty that require additional exploration. The scatter in Figures 2 through 4 suggests that the inclusion of statistical and visual exclusion criteria influence g only slightly, yet they do reduce the standard deviations. Uncertainties associated with the assigned exclusion thresholds, in particular the visual inspection, have yet to be quantified. Several components of the atmospheric correction process have empirical components, such as the calculation of f_b and f_λ and an additional correction for non-negligible L_w(NIR)[10], yet their contributions to the uncertainty budget have yet to be quantified as well. The latter are inherent to the instrument-atmospheric correction system, and thus, relevant to the generic application of our approach. For the particular case of the operational OBPG $\overline{g}$ calculation for SeaWiFS and MODIS-Aqua, however, uncertainties associated with the acquisition and processing of MOBY L_{wn}^{t} have yet to be documented. While a detailed review of the latter is beyond the scope of this work, subsequent related analyses would greatly improve our ability to accurately vicariously calibrate on-orbit ocean color sensors.

REFERENCES

1. Tomlinson, M.C. and 7 co-authors (2004). Evaluation of the use of SeaWiFS imagery for detecting *Karenia brevis* harmful algal blooms in the eastern Gulf of Mexico. *Remote Sensing of Environment*, 91, 293-303.

2. Antoine, D.A. and 4 co-authors (2005). Bridging ocean color observations of the 1980s and 2000s in search of long-term trends. *Journal of Geophysical Research*, 110, doi:10.1029/2004JC002620.

3. Gordon, H.R. (1998). In-orbit calibration strategy for ocean color sensors. *Remote Sensing of Environment*, 63, 265-278.

4. Eplee, Jr., R.E. and 7 co-authors (2001). Calibration of SeaWiFS. II. Vicarious techniques. *Applied Optics*, 40, 6701-6718.

5. Gordon, H.R. and Wang, M.H. (1994). Retrieval of water-leaving radiance and aerosol optical-thickness over the oceans with SeaWiFS – a preliminary algorithm. *Applied Optics*, 33, 443-452.

6. Gordon, H.R. (1997). Atmospheric correction of ocean color imagery in the earth observing era. *Journal of Geophysical Research*, 102, 17081-17106.

7. Hooker, S.B. and 5 co-authors (1992). *An overview of SeaWiFS and Ocean Color*. NASA Tech. Memo. 104566 Vol. 1, NASA Goddard Space Flight Center, Greenbelt, Maryland, pp. 24.

8. Barnes, R.A. and 7 co-authors (2004). Comparison of SeaWiFS measurements of the Moon with the U.S. Geophysical Survey lunar model. *Applied Optics* 43, 5838-5854.

9. Clark, D.K. and 5 co-authors (1997). Validation of atmospheric correction over oceans. *Journal of Geophysical Research*, 102, 17209-17217.

10. Patt, F.S, and 17 co-authors (2003). *Algorithm Updates for the Fourth SeaWiFS Reprocessing*. NASA Tech. Memo. 206892 Vol. 22, NASA Goddard Space Flight Center, Greenbelt, Maryland, pp. 74.

11. Franz, B.A. and 9 co-authors (2005). The continuity of ocean color measurements from SeaWiFS to MODIS. In J.J. Butler (Ed.), *Proceedings SPIE Vol. 5882*, doi:10.1117/12.620069.

12. Morel, A., Antoine, D., and Gentili, B. (2002). Bidirectional reflectance of oceanic waters: accounting for Raman emission and varying particle scattering phase function. *Applied Optics*, 41, 6289-6306.

13. O'Reilly, J.E. and 24 co-authors (2000). *SeaWiFS Postlaunch Calibration and Validation Analyses, Part 3*. NASA Tech. Memo. 206892, Vol. 11, NASA Goddard Space Flight Center, Greenbelt, Maryland, pp 24.

14. Martiny, N., Frouin, R., and Santer, R. (2005). Radiometric calibration of SeaWiFS in the near infrared. *Applied Optics*, 44, 7828-7844.

15. Barnes, R.A. and 7 co-authors (2000). The calibration of SeaWiFS on orbit. In W.L. Barnes (Ed.), *Proceedings of SPIE Vol. 4135*, 281-293.

16. Wang, M. and Gordon, H.R. (2002). Calibration of ocean color scanners: how much error is acceptable in the near infrared? *Remote Sensing of Environment*, 82, 497-504.

17. Fargion, G.S., Barnes, R.A., and McClain, C.R. (2001). *In situ Aerosol Optical Thickness Collected by the SIMBIOS Program (1997-2000): Protocols, Data QC, and Analysis*. NASA Tech. Memo. 209982, NASA Goddard Space Flight Center, Greenbelt, Maryland, pp. 109.

18. Mueller, J.L. and 26 co-authors (2003). *Ocean Optics Protocols for Satellite Ocean Color Sensor Validation, Vol. 6, Rev. 4: Special Topics in Ocean Optics Protocols and Appendices*. NASA Tech. Memo. 211621, NASA Goddard Space Flight Center, Greenbelt, Maryland, pp 148.

19. Bailey, S.W. and Werdell, P.J. (2006). A multi-sensor approach for the on-orbit validation of ocean color satellite data products. *Remote Sensing of Environment*, 102, 12-23.

TABLES

Table 1. Variable symbols and their definitions.

Symbol	Description
f_p	polarization correction factor
f_s	Earth-Sun distance correction factor
f_λ	band-pass adjustment correction factor
f_b	bidirectional reflectance correction factor
g	vicarious gain for a single observation
$\overline{g}$	mean vicarious gain for all observations
L_t	radiance observed at the top of the atmosphere
L_r	radiance due to Rayleigh scattering from air molecules
L_a	radiance due to scattering by aerosols, including Rayleigh-aerosol interactions
L_f	radiance due to white caps and foam at the sea surface
L_w	water-leaving radiance
L_{wn}	normalized water-leaving radiance
s	subscript denoting solar path
t	superscript denoting a predicted value
t_g	transmittance due to gaseous absorption (e.g., ozone)
t_d	Rayleigh-aerosol diffuse transmittance
v	subscript denoting sensor view path
θ	cosine of zenith angle

Table 2. Proposed SeaWiFS visible and NIR vicarious gains ($\overline{g}$) and standard deviations (s) for the upcoming Reprocessing 6 (Spring 2007). The sample size is 60.

	412	443	490	510	555	670	765	865
$\overline{g}$	1.0324	1.0086	0.9887	0.9955	0.9967	0.9654	0.9645	1
s	0.010	0.009	0.007	0.007	0.008	0.005	0.004	0

Table 3. MODIS-Aqua visible and NIR vicarious gains ($\overline{g}$) and standard deviations (s) for Reprocessing 1.1 in August 2005. The sample size is 20.

	412	443	488	531	551	667	678	748	870
$\overline{g}$	0.9710	0.9848	0.9795	0.9870	0.9850	0.9797	0.9776	0.9855	1
s	0.006	0.005	0.005	0.005	0.005	0.003	0.004	0.004	0

Table 3. Regression statistics for SeaWiFS (reprocessed using $\overline{g}$) versus MOBY L_{wn}, for the observations used to calculate $\overline{g}$. N is sample size, RMS is root mean square (standard deviation), and MPD is absolute median percent difference.

	412	443	490	510	555	670
N	60	60	60	60	60	60
r^2	0.96	0.91	0.73	0.50	0.41	0.36
slope	1.06	1.06	1.05	1.14	1.47	5.07
intercept	-0.10	-0.07	-0.05	-0.08	-0.12	0.07
RMS	0.053	0.052	0.038	0.035	0.024	0.009
bias	0.02	0.02	0.01	0.01	0.00	0.00
MPD	2.1	1.9	2.2	3.1	5.4	37.2
ratio	1.008	1.011	1.009	1.010	1.003	1.081

Table 4. SeaWiFS visible and NIR vicarious gains ($\overline{g}$) and standard deviations (s) calculated without the bidirectional reflectance correction[12] applied (f_b set to unity). The sample size remains 60. The percent differences (%) relative to the operationally processed gains (Table 2) are also provided.

	412	443	490	510	555	670	765	865
$\overline{g}$	1.0251	1.0006	0.9803	0.9891	0.9925	0.9643	0.9645	1
s	0.007	0.008	0.007	0.007	0.007	0.005	0.004	
%	-1.05	-1.19	-1.08	-0.65	-0.14	0.17		

FIGURES

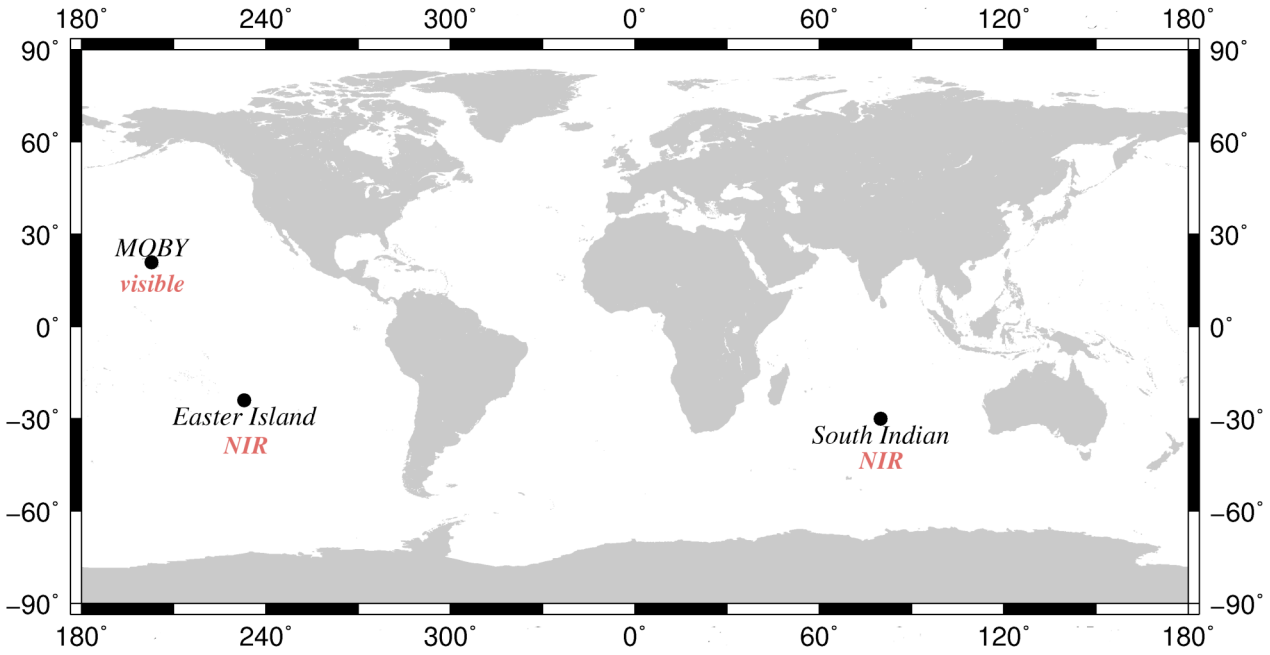

Figure 1. The current OBPG vicarious calibration sites.

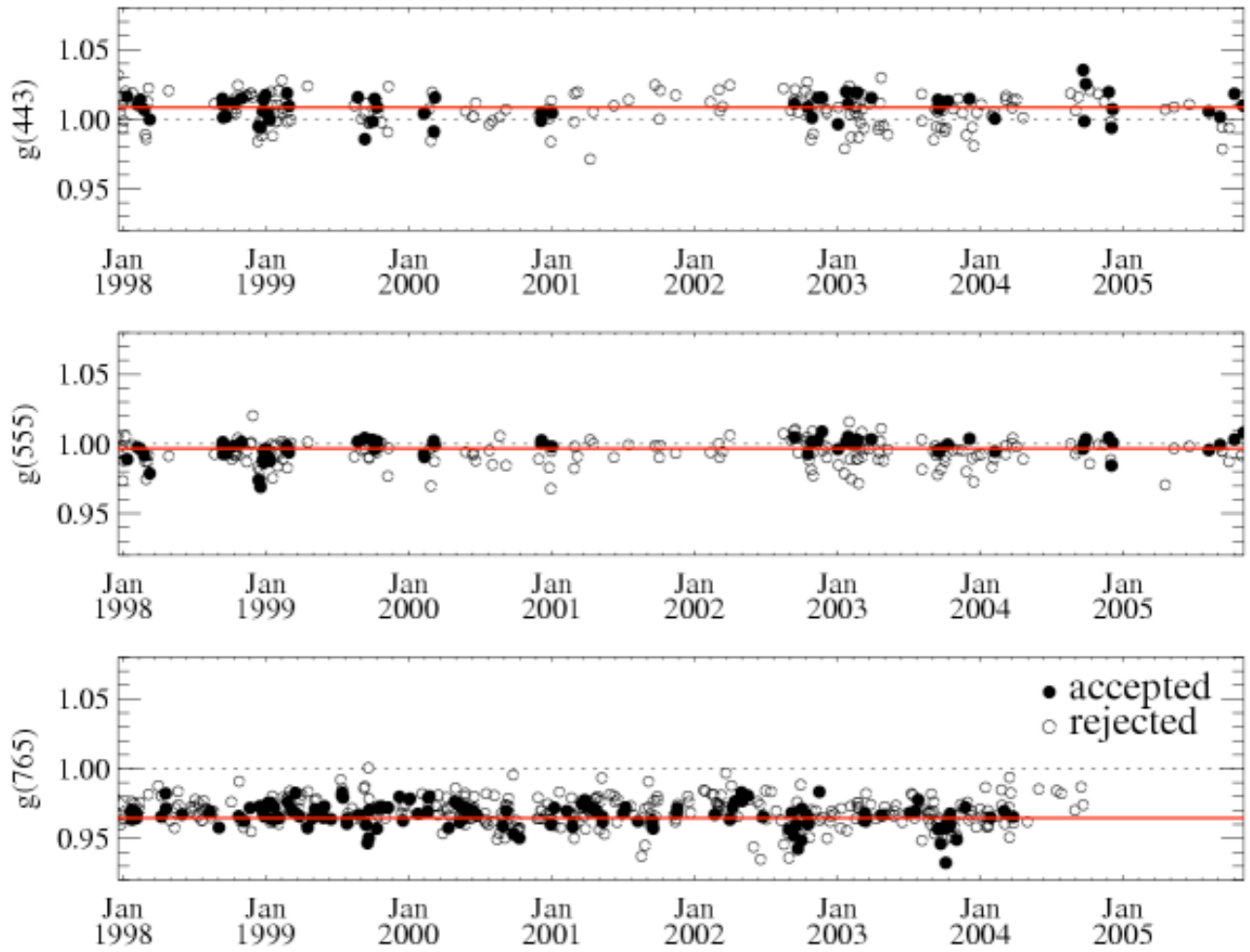

Figure 2. SeaWiFS g (circles) and $\bar{g}$ (red line) as a function of time.

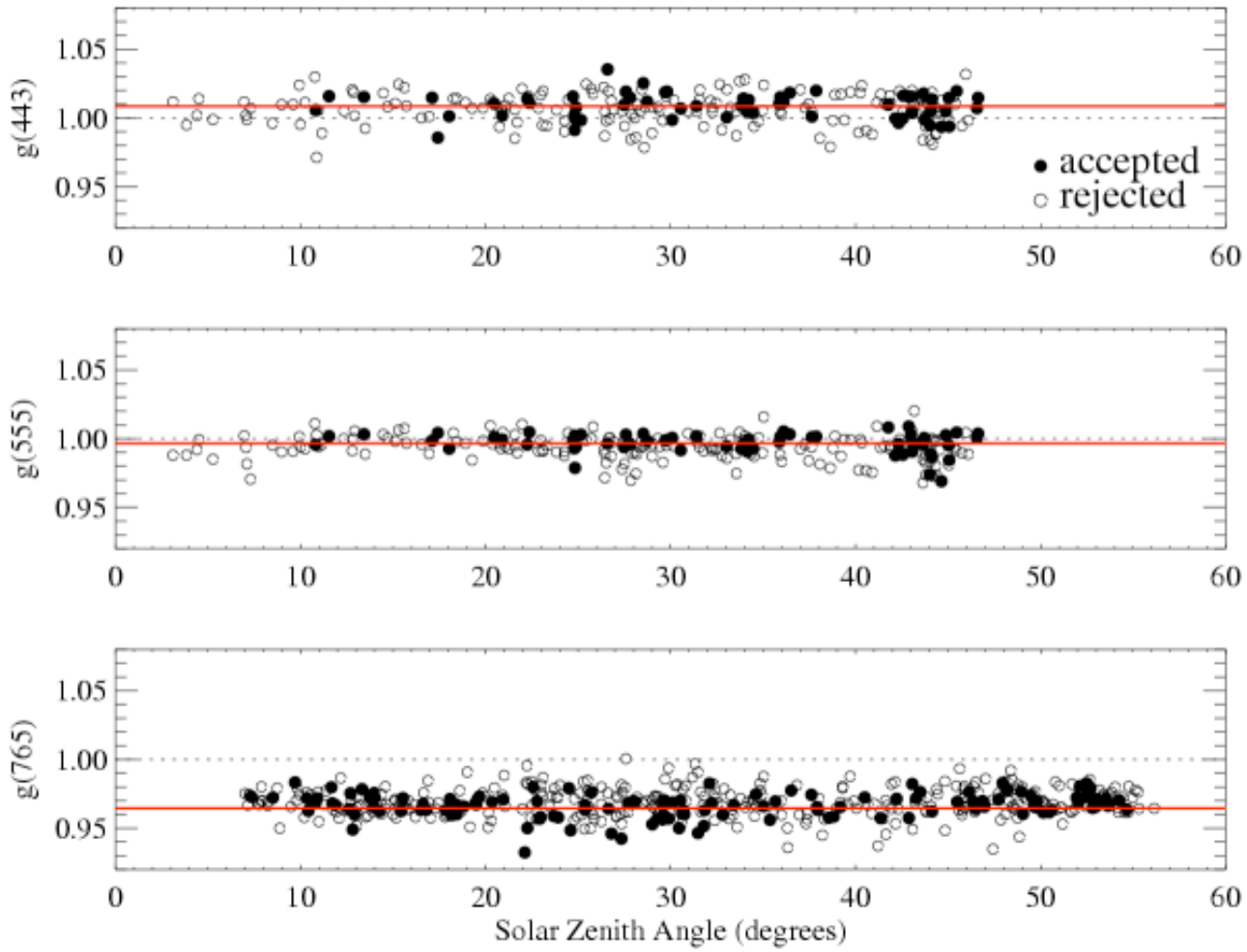

Figure 3. SeaWiFS g (circles) and $\bar{g}$ (red line) as a function of solar zenith angle.

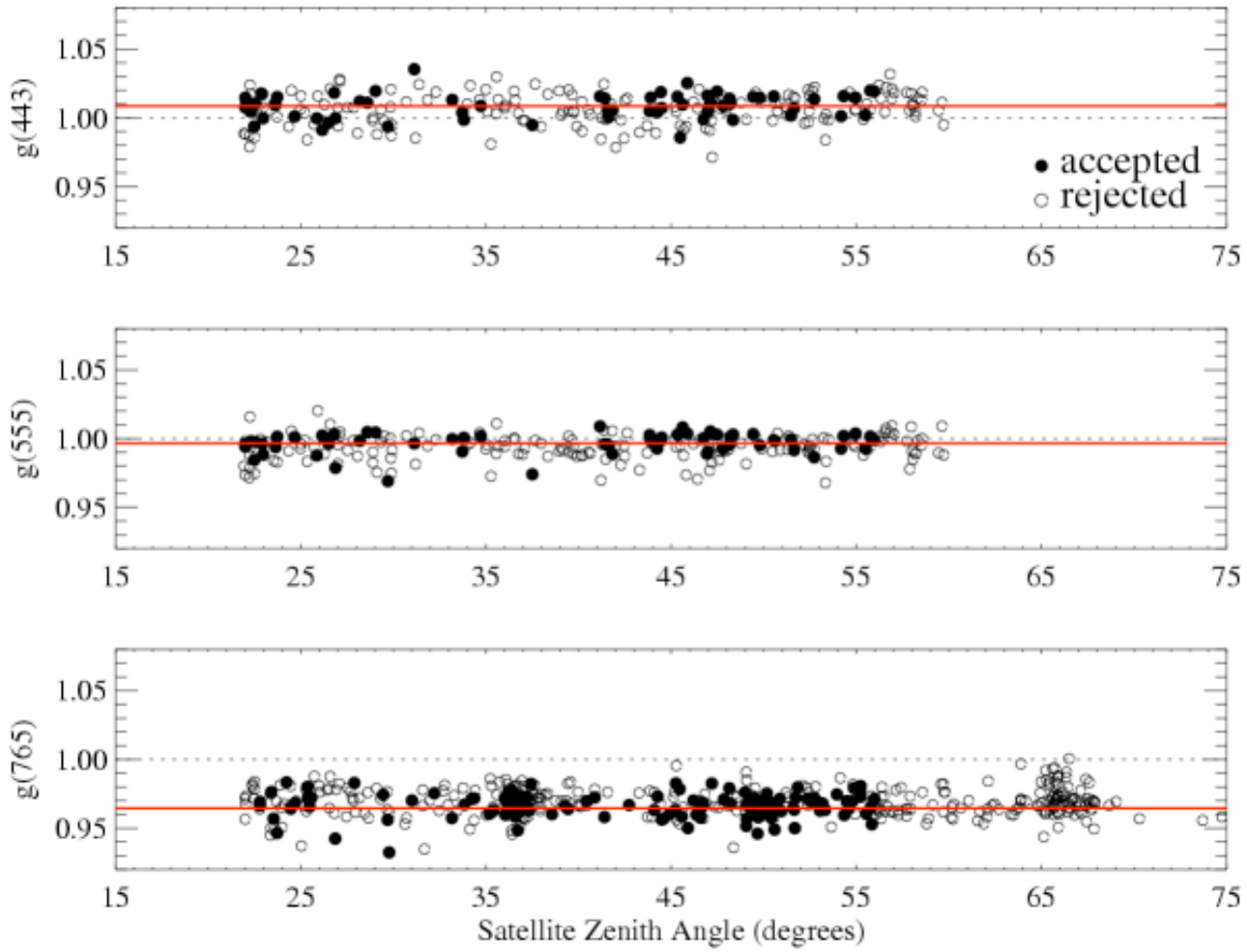

Figure 4. SeaWiFS g (circles) and $\bar{g}$ (red line) as a function of satellite zenith angle.

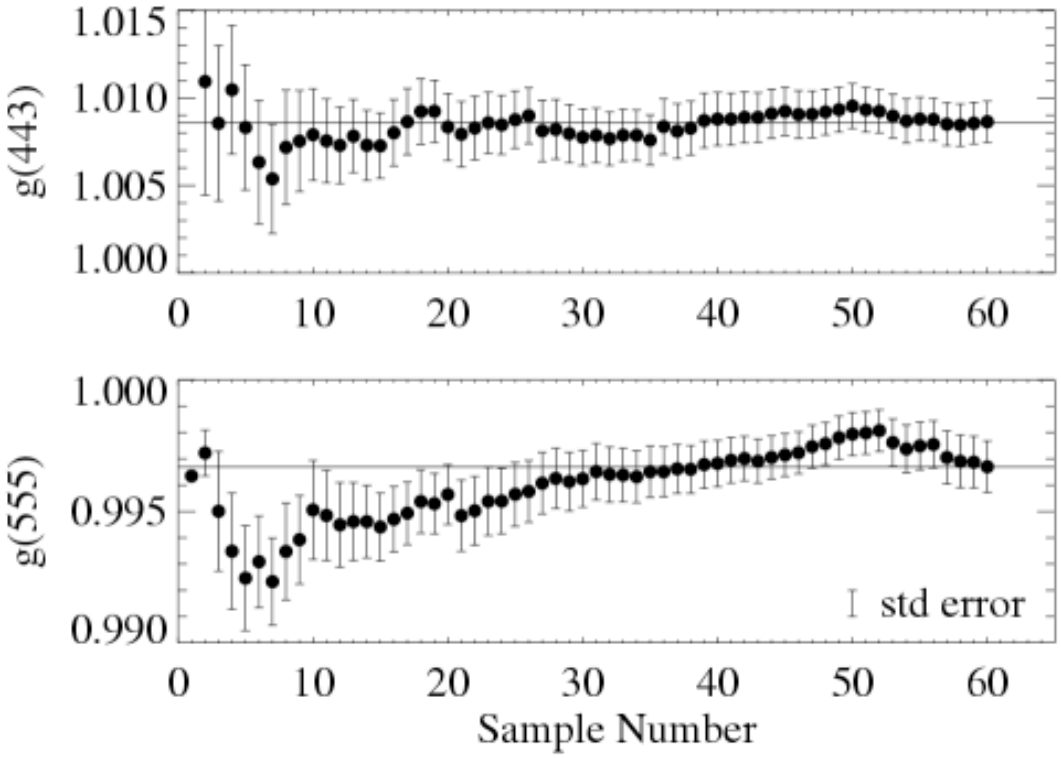

Figure 5. SeaWiFS $\overline{g}$ and standard deviation (error) as a function of sample size. Samples are sorted by time (8-years of observations from 1998-2005). The solid horizontal line indicates the final $\overline{g}$.